Does printing direction influence the bond between 3D printed polymeric reinforcement and cementitious matrix?

Bol, Rowin J.M.; Xu, Yading; Luković, Mladena; Šavija, Branko

DOI
10.1016/j.engfailanal.2025.109471

Publication date
2025

Document Version
Final published version

Published in
Engineering Failure Analysis

Engineering Failure Analysis 174 (2025) 109471

Contents lists available at ScienceDirect

Engineering Failure Analysis

journal homepage: www.elsevier.com/locate/engfailanal

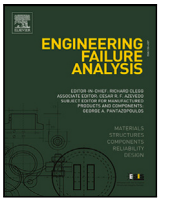

Does printing direction influence the bond between 3D printed polymeric reinforcement and cementitious matrix?

Rowin J.M. Bol [a,*], Yading Xu [a], Mladena Luković [b], Branko Šavija [a]

[a] Microlab, Faculty of Civil Engineering and Geosciences, Delft University of Technology, Stevinweg 1, 2628 CN Delft, The Netherlands
[b] Concrete Structures Group, Faculty of Civil Engineering and Geosciences, Delft University of Technology, Stevinweg 1, 2628 CN Delft, The Netherlands

ARTICLE INFO

Keywords:
3D printed reinforcement
Additive Manufacturing (AM)
Bond behaviour
Numerical simulation
Lattice Beam Model (LBM)

ABSTRACT

The use of 3D printed polymers in the form of lattice reinforcement can enhance the mechanical properties of cementitious composites. Methods like Fused Deposition Modelling (FDM) 3D printing enable their creation, but this process has a large (negative) effect on their mechanical properties, with a large dependency on the printing direction. Continuing on our previous study concerned with modelling the anisotropic behaviour of 3D printed polymeric reinforcement, this work focuses on the reinforcement-matrix bond. Because of the layer-by-layer filament extrusion process of the 3D printing technique, the edges of FDM 3D printed polymers are typically composed of ellipses. Based on this, it is hypothesized that morphological effects as a result of the 3D printing technique enhance the bond between 3D printed reinforcement and cementitious matrix: The elliptic geometry potentially facilitates interlocking with the cementitious mortar, thereby possibly enhancing the bond behaviour in certain directions. To investigate the geometrical directional-dependent features at the edges of 3D printed polymers in more detail, micro-scale models are developed. Geometrical effects induced by different printing configurations are studied. The simulation results are verified through meso-scale pull-out experiments. The interlocking effects as a result of the 3D printing technique show to be significant seeing a bond strength increase of up to 56 % in one of the print configurations compared to the direction without any geometrical effects.

1. Introduction

3D printed polymers in the form of lattice reinforcement can enhance the properties of cementitious composites [1–3]. One of the considered composite categories exhibits excellent compressive ductility, which is achieved by auxetic reinforcement architectures [4]. These auxetic architectures are mechanical metamaterials which have a negative Poisson's ratio [5–18]. Additive Manufacturing (AM) methods like 3D printing enable the creation of auxetic structures [7]. However, the production process of such reinforcements has a large effect on their mechanical properties, with a large dependency on the direction of printing and loading [19]. Some concerns for objects constructed through AM are, for instance, the containing of geometrical imperfections [14] and high level of anisotropy [9].

Our literature review on micromechanical models for 3D printed polymers, focusing on Fused Deposition Modelling (FDM), covers numerous literature on the topic of so-called *printing process parameters*, elaborating their influences on mechanical properties and behavioural features [20]. Among the investigated process parameters for FDM are surface roughness and quality (e.g. [21–26]).

* Corresponding author.
E-mail address: R.J.M.Bol@tudelft.nl (R.J.M. Bol).

https://doi.org/10.1016/j.engfailanal.2025.109471
Received 13 December 2024; Received in revised form 21 February 2025; Accepted 27 February 2025
Available online 7 March 2025

Surface roughness, also described as surface quality, is related to the layer-by-layer filament extrusion process of the 3D printing technique. Therefore, the edges of FDM 3D printed polymers are typically composed of ellipses [27]. These can be regarded as superficial defects, because the intended shapes, usually modelled through 3D software, do not contain these edge effects [26]. As a result, the elliptic exterior surfaces of FDM 3D printed polymers include variations [27], which can be seen as 'porosity of the edges' [20].

Based on the review by Bol & Šavija [20], it is hypothesized that morphological effects as a result of the 3D printing technique may enhance the bond behaviour between FDM 3D printed reinforcement and cementitious matrix: The elliptic geometry potentially facilitates interlocking with the cementitious mortar, thereby possibly enhancing the bond behaviour in certain directions. This, in combination with our previous work on printing path-dependent two-scale models for 3D printed planar auxetics by material extrusion (i.e. FDM) [28], is the next step in our development of a modelling framework for simulating deformation and fracture of Auxetic Cementitious Composites (ACCs). In the aforementioned reference, we propose an experimentally validated two-scale model that is able to capture the *printing path-dependent anisotropy* of 3D printed polymers using the Lattice Beam Model (LBM). So far, the bond behaviour in LBM simulations for reinforced cementitious composites was considered either by parameter fitting [29,30] or through analytical expressions [31,32]. More recently, Mustafa et al. [33] determined the concrete–reinforcement interface element properties via inverse analysis to get the same crack widths as experimentally measured, and Gu et al. [34] proposed a generalized mathematical approach to model reinforcement–concrete bond.

The current paper provides valuable insights regarding the effect of printing direction on the interface properties between 3D printed reinforcement and cementitious matrix. Using a novel approach to model pull-out experiments on two different length scales, this study offers a good understanding of bond properties between 3D printed reinforcement and cementitious matrix at the micro-scale. Microscopic investigations of failure mechanisms in additively manufactured reinforcement as well as amongst 3D printed reinforcement and cementitious matrix are considered. Failure analysis for a 3D printed polymeric-cementitious composite system is performed with numerical simulations. To the best of the authors' knowledge, this work is the first to quantitatively investigate the influence of printing direction on the bond between 3D printed polymeric reinforcement and cementitious matrix. A novel methodology for determining the bond between cementitious matrix and 3D printed polymers is explained, starting with pull-out experiments between FDM 3D printed Acrylonitrile Butadiene Styrene (ABS) bars and cementitious mortar (described in [35]), which are used to calibrate a meso-scale pull-out model. Morphological effects are studied by numerical simulations on two length scales, leading to a good understanding of the effects the geometrical directional-dependent edge features of 3D printed polymers have on the bond behaviour. Bond properties are first determined at the meso-scale using a pull-out model which resembles the pull-out experiments (as described in [35]). It should be noted, however, that these pull-out tests are performed on ABS bars in which the printing path is parallel to the direction of loading to avoid any influence from the intra-layer and inter-layer bonds caused by the printing process. Monaldo & Marfia [36] describe the inter-layer bond as cohesion among layers stacked vertically during the printing process, and the intra-layer bond as cohesion among filaments deposited next to each other horizontally within the same layer (see Fig. 6). Secondly, to explicitly model the geometrical directional-dependent features at the edges of FDM 3D printed polymers, micro-scale models are developed using the meso-scale properties as a reference. The material properties of the ABS bars for both the meso-scale and micro-scale models are adopted from our previous work [28] and are calibrated based on experimental results.

2. Literature

2.1. Reinforcement-matrix bond behaviour

The bond between cementitious materials and reinforcement has been investigated for almost 150 years since Hyatt [37] performed tests on concrete and iron bars as early as 1876 [38]. This action of force transfer plays a crucial role in the performance of Reinforced Concrete (RC) elements [39–41]. Bond properties significantly affect the structural response of RC members, such as their load-carrying capacity (i.e. strength), crack propagation, crack widths, and deformation capacity and seismic resistance (i.e. energy absorption and dissipation capacity) [34,40]. It is therefore essential to provide accurate constitutive relationships for interface elements in numerical simulations of RC structures [34,42]. Although extensively researched by both experimental and analytical means [39], the bond between cementitious materials and reinforcement remains complex because of its dependency on numerous parameters (e.g. cover thickness, confinement conditions and concrete strength) [34].

Generally, bond behaviour can be defined as the force transfer or shear stress between concrete and reinforcement [43]. The term *bond stress* is often used to describe this shear stress or unit shear force that acts parallel to a reinforcement bar on its interface with surrounding concrete [44]. The bond transfers the reinforcement bar forces to the cementitious matrix, or vice versa, by which the bond stress alters the steel stress: '(...) there can be no bond stress unless the bar stress changes, and there can be no change in bar stress without bond stress.' [44]. As defined by the American Concrete Institute (ACI), bond is composed of the following three constituents (Fig. 1): (i) chemical adhesion between the concrete and the reinforcement bar; (ii) friction as a result of interfacial surface roughness, transverse forces exerted on the bar, and relative slip between the concrete and the reinforcement bar; and (iii) mechanical interaction between the cementitious matrix and steel by means of anchorage or interlocking of the surrounding concrete and ribs on deformed reinforcement bars [43,45]. Moreover, it is asserted that the bond stress varies with respect to the *bond slip*, which represents the difference in displacements between the concrete and reinforcement [39]. It is this bond slip that causes local concrete failure, which in turn deteriorates the bond behaviour.

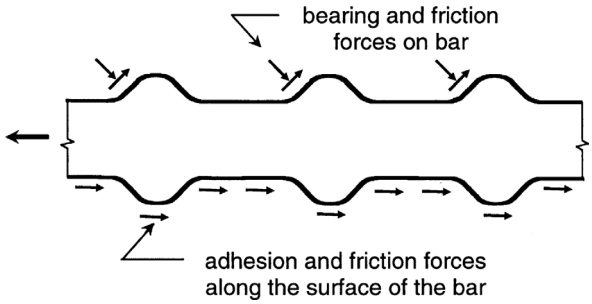

Fig. 1. Bond force transfer mechanisms [45].

2.2. Experimental contributions

Various test setups can be utilized for investigating the bond between concrete and (deformed) reinforcement bars [45]. Due to its convenient manufacturing and straightforward testing procedure [39], the majority of experiments for obtaining bond are performed using a pull-out set-up [45]. In these tests, a reinforcement bar is embedded in a concrete cylinder or prism and directly pulled out from one end whilst the matrix is held in place from the same side [44]. However, it is argued in several studies (e.g. [39,45]) that the pull-out configuration is not representative or even unrealistic because of its boundary conditions: the compressive reaction stresses in the concrete near the supports cause an induced confinement of the interface, which is not present in most RC members. American Concrete Institute (ACI) Committee 408 [45] therefore discourages the use of this testing configuration. This view is supported in [46] for deformed reinforcement bars, where it is remarked that pull-out tests typically overestimate the bond capacity. Nevertheless, the latter reference also reflects on the case for plain reinforcement bars for which it is concluded that pull-out tests capture the actual failure mode and enable for precise evaluation of their bond behaviour as these do not (primarily) rely on mechanical interlock.

After the occurrence of slip, the bond stress along the reinforcement bar is assumed to be uniform. In view of this, most (experimental) studies consider a bond unit stress (e.g. [29,38,44,46,47]):

$$\tau = \frac{P}{mh} = \frac{P}{\pi d L}\,, \tag{1}$$

where τ is the nominal (average) bond stress or interfacial shear stress, P is the applied pull-out load or reinforcement bar force, $m = \pi d$ the circumference of the reinforcement bar, d the reinforcement bar diameter, and h and L are the embedded length (sometimes simply equal to the specimen length [38,44], depending on the reference and test setup).

Recent developments have led researchers to study the mechanical bonding of the interface between cementitious matrix and 3D printed polymer material as reinforcement in composites, such as the work by Namakiaraghi et al. [48]. In particular, they investigate the influence of surface texture on the bond behaviour by means of performing pull-out experiments on rectangular 3D printed PLA specimens having smooth and textured exterior surfaces (see Fig. 2). Their experimental campaign involves specimens having two rectangular dimensions (D) of 5×5 and 6.75×6.75 mm^2, as well as five different embedded lengths (L) equal to $2D$, $6D$, $10D$, $14D$, and $18D$. Results indicate that larger tensile stresses need larger embedded lengths to prevent bond failure and that if the PLA specimens broke before pull-out, bond stresses are proportional with the embedded length L. The exterior surface texture has a positive effect on the bond behaviour such that equal embedded lengths can sustain higher tensile stresses compared to the smooth specimens. This means that a rough surface results in a stronger bond than a smooth surface. Through extrapolating fitted linear regression curves critical bond lengths (l_c) are found, which are explained as a lower bound for when tensile stresses cause rupture of the 3D printed material instead of pull-out. Phrased differently, one should ensure that $l \geq l_c$ to exploit the reinforcement to its full potential. Using the experimental data and determined critical bond lengths, shear bond strengths are computed as:

$$\tau = \frac{P_{\max}}{\pi d l_c}\,, \tag{2}$$

where $P_{\max}$ is the maximum force measured upon breaking of the bond at l_c, and d the rectangular specimen dimension. Bond strengths of 0.76, 0.67, and 1.35 MPa were found for specimens having 5 and 6.25 mm smooth, and 6.75 mm textured exterior surfaces, respectively. Similar to conventional reinforcement (i.e. ribbed steel reinforcement bars), this points out that the mechanical bonding of the interface between cementitious matrix and 3D printed polymer material is dependent on both the embedded length and the surface texture, where the latter facilitates a significant raise in bond strength of over 100%. Finally, Namakiaraghi et al. [48] also consider, both experimentally and numerically, flexural beam specimens. Bond behaviour is related then to the fact whether the surface texture of the reinforced samples are smooth or having vertical anchorage of the PLA reinforcement. These are found to exhibit the same characteristics as plain mortar beams up to initial cracking, however, the anchored beams regain their strength by over 250% and show ultimate mid-span deflections reaching more than ten times that of plain mortar before failure of the reinforcement. However, in their numerical models of the flexural beam specimens Namakiaraghi et al. [48] assume no bond failure will occur before the PLA reinforcement fails. They reason that the Young's moduli of the cementitious matrix and 3D printed material have the same order of magnitude, as opposed to conventional RC beams, and therefore argue that no slipping

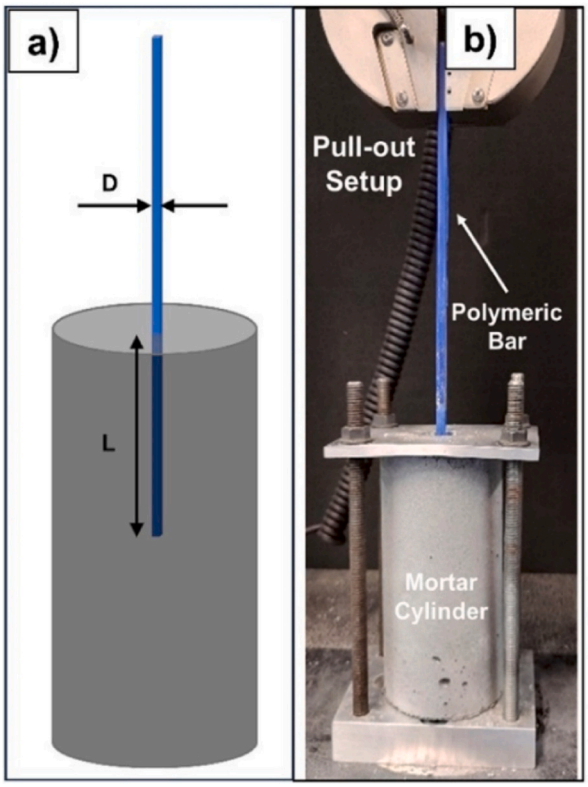

Fig. 2. Pull-out experiments on rectangular 3D printed PLA specimens having varying diameters (D) and embedded lengths (L): (a) Schematic, (b) Setup [48].

nor detachment of the reinforcement will occur. Instead, it is discussed that both materials are likely to mutually fail such that the bond behaviour can be modelled using the Embedded Region (ER) constraint available in commercially available FEM software (e.g. ABAQUS Explicit). Nevertheless, this constraint does not enable the implementation of a bond stress–slip relationship between cementitious matrix and 3D printed polymer material.

2.3. Analytical models

Experimental results are often generalized in terms of analytical models that represent the observed behaviour in a mathematical manner. This is mainly done to quantify these relationships under different boundary conditions [34]. A large number of analytical models has been developed that describe the bond behaviour between concrete and deformed reinforcement bars (e.g. [40,42,44,47,49,50]). A recent study by Gu et al. [34] proposed a methodology for LBM simulations to determine the mechanical properties (strength and Young's modulus) of interface elements between concrete and deformed reinforcement bars. Therein, a particularly interesting analytical model by Harajli et al. [40,47,50] was used. The analytical model is graphically displayed in Fig. 3. The analytical model shows similarities with one previously proposed by Eligehausen et al. [49]. It can be seen that the pull-out envelope consists of four phases, starting with an ascending branch that was derived using similar experiments as performed by Eligehausen et al. [49].

3. Methodology

Determining the bond behaviour between cementitious mortar (i.e. matrix) and 3D printed polymers (e.g. ABS) is relevant for all cases where 3D printed reinforcement is used in cementitious composites. In fact, it is a crucial intermediate step when moving from solely modelling 3D printed polymeric reinforcement architectures (see [28]) towards modelling composites. Therefore, it is important that this behaviour is implemented into numerical simulations. The starting point for this are pull-out experiments between FDM 3D printed ABS bars and cementitious mortar (described in [35]), which are used to calibrate a meso-scale pull-out model. From this meso-scale bond model, the calibrated bond properties could be directly used in specimen-scale models for simulating the composite behaviour of cementitious mortar reinforced with auxetic architectures like the Re-Entrant (RE) and Rotating Square (RS) designs in [28]. However, based on our literature review [20], as well as the Scanning Electron Microscope (SEM) pictures in Fig. 4, it is hypothesized that morphological effects as a result of the 3D printing technique may have a beneficial effect on the bond behaviour between FDM 3D printed polymers and cementitious matrix.

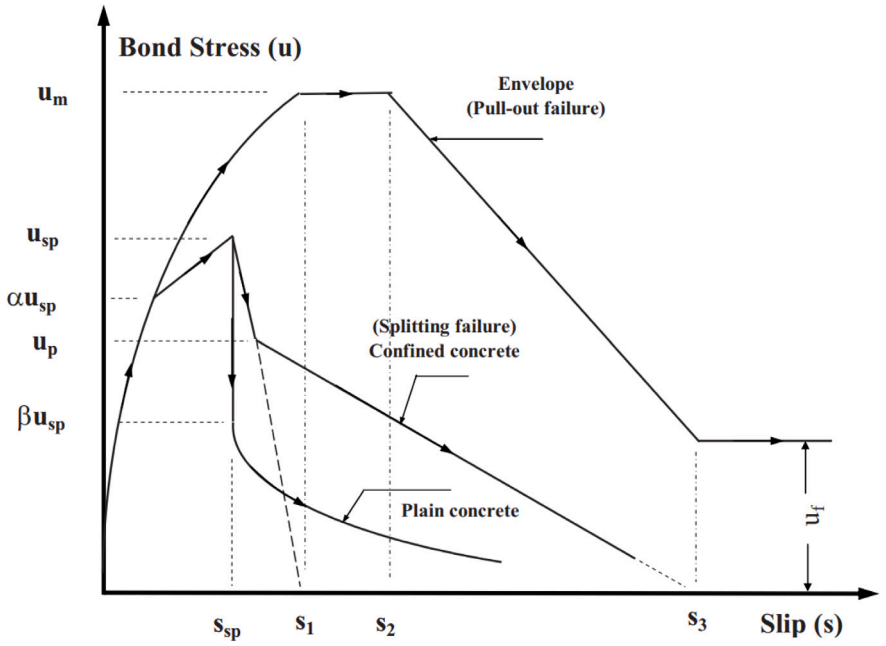

Fig. 3. Monotonic envelope model [50].

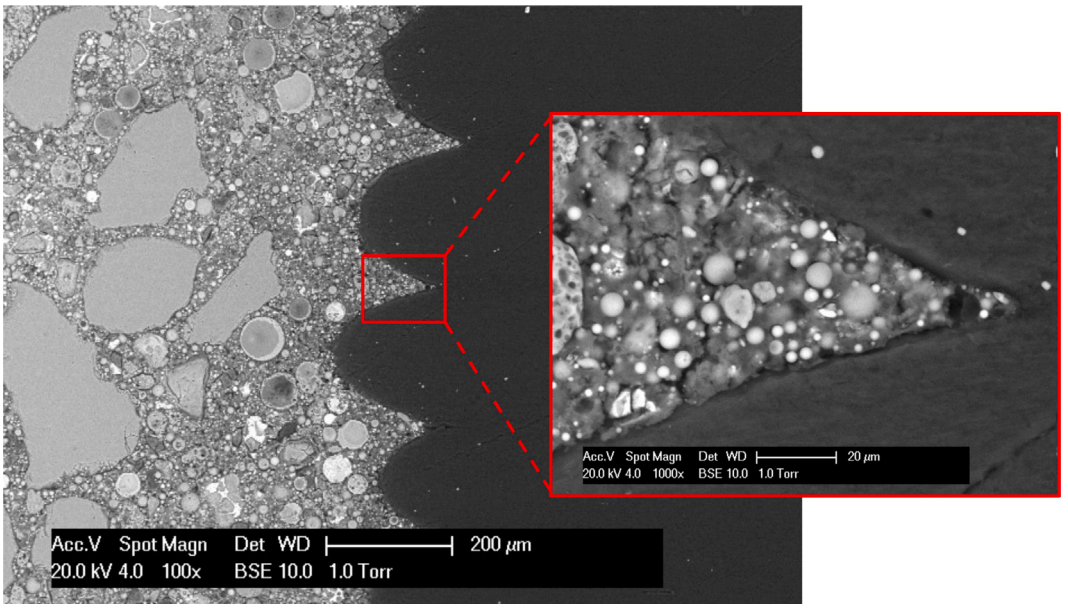

Fig. 4. SEM picture of the interface between FDM 3D printed ABS and cementitious mortar before failure.

To study the influence of these morphological effects on the bond behaviour, numerical simulations on two length scales using LBM simulations are proposed in this section. To begin with, bond properties shall be determined on the meso-scale using a pull-out model which resembles the pull-out experiments (as described in [35]). These pull-out tests are performed on ABS bars in which the printing path is parallel to the direction of loading to avoid any influence from the intra-layer and inter-layer bonds caused by the printing process, see Fig. 6. In other words: the pull-out behaviour is experimentally measured in the bead or filament direction (i.e. the 'bulk material' without interfaces perpendicular to the loading direction, see [20]).

Table 1
Printing parameters from our previous study [35].

Parameters	Configuration
Nozzle diameter (mm)	0.8
Temperature (°C)	260
Layer height (mm)	0.2
Line width (mm)	0.7
Infill density (%)	100
Printing speed (mm s^{-1})	40

Table 2
Mixture design of cementitious matrix from our previous study [35].

Mixture components	Quantities (g L^{-1})
CEM I 42.5 N	550
Fly ash	650
Sand (0.125–0.250 mm)	550
Superplasticizer (Glenium 51)	2
Water	395

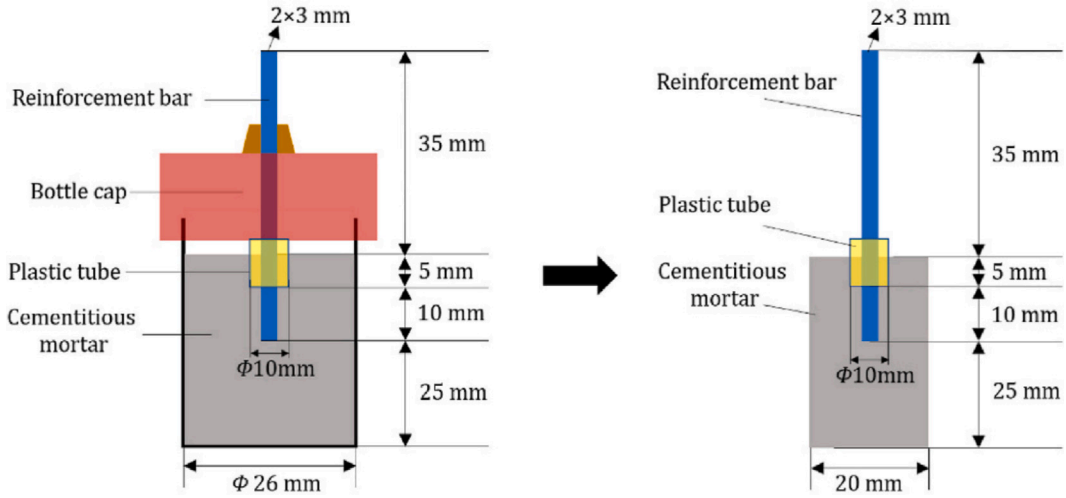

Fig. 5. Bars fixed in cylindrical moulds (left) and dimensions of the prismatic pull-out specimens after cutting (right) [35].

3.1. Experimental analysis

The mix design of the mortar with a water to cement ratio of 0.33 therein was taken from [51] as provided in Table 2 and tested after 28 days. The experimental pull-out results are adopted from our previous work [35] in which four specimens were created by a commercially available FDM 3D printer (Ultimaker 2+) provided the printing parameters in Table 1. The resulting 2 × 3 mm ABS bars with a length of 50 mm were placed in plastic cylindrical moulds having a radius of 10 mm. To prevent any boundary effects near the bonded region, the first 5 mm of the cementitious cylinder was prevented to touch the ABS bar by means of a plastic tube with a radius of 5 mm, while the embedded length was 10 mm. When cured and demolded, the specimens were cut into rectangular pull-out samples. The creation and dimensions of the pull-out specimens are depicted in Fig. 5. All experiments were conducted in our laboratory at room temperature.

The pull-out tests were executed by a hydraulic press INSTRON 8872, in which the cementitious cylinders were installed upside down within the steel loading frame of the device (see Fig. 6). The ABS bars were loaded by means of a clamp that was fixed to the hydraulic press and displaced at a rate of 5×10^{-3} mm s^{-1}. The force and deformation recordings were performed through the INSTRON itself and Linear Variable Differential Transducers (LVDTs) at both sides of the clamp, respectively, as shown in Fig. 6.

Experimental pull-out results [35] are presented as bond stress–slip curves in Fig. 8. The bond stress in Fig. 8 is calculated using the actual circumference obtained from the expanded geometrical model described in [28] as shown in Fig. 7. This model describes the cross-sectional shape of 3D printed materials and requires the following input parameters: the layer thickness (t), vertical overlap interval (c), air gap (H), raster orientation (β), cross-sectional shape parameters (a, b) or the ratio between the bead's semi-major and semi-minor axes ($r = a/b$), the layer width (L), horizontal overlap interval (d), inter-layer bond width (w_{inter}), and intra-layer bond height (h_{intra}). The average input parameters for the extended geometrical model shown in Fig. 7 as obtained from the microstructural experimental analysis performed in [28] are listed in Table 3.

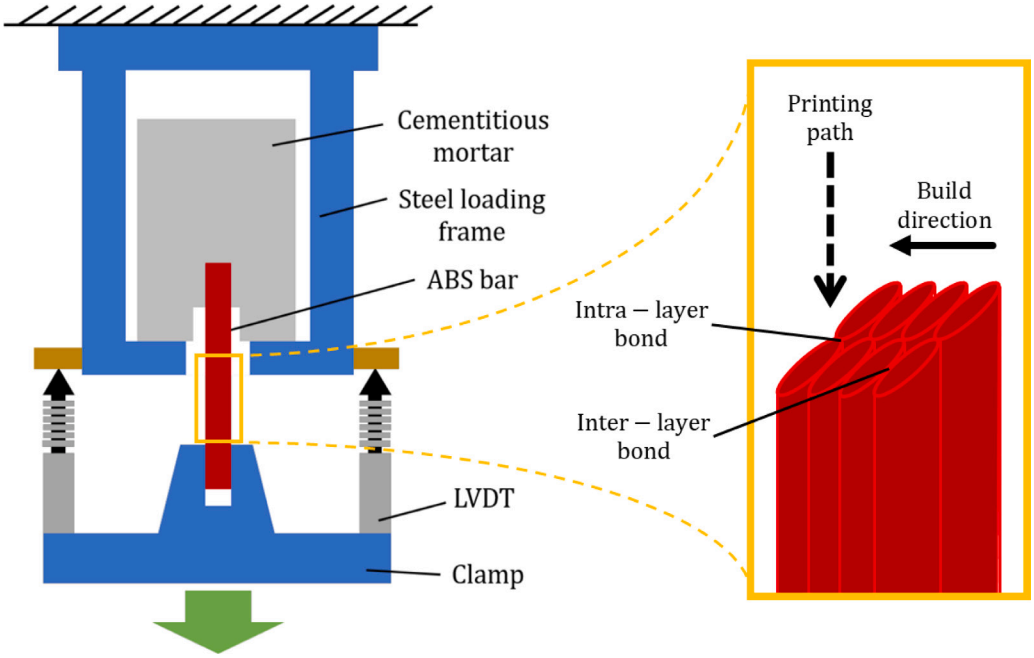

Fig. 6. Schematics of the pull-out test set-up [35].

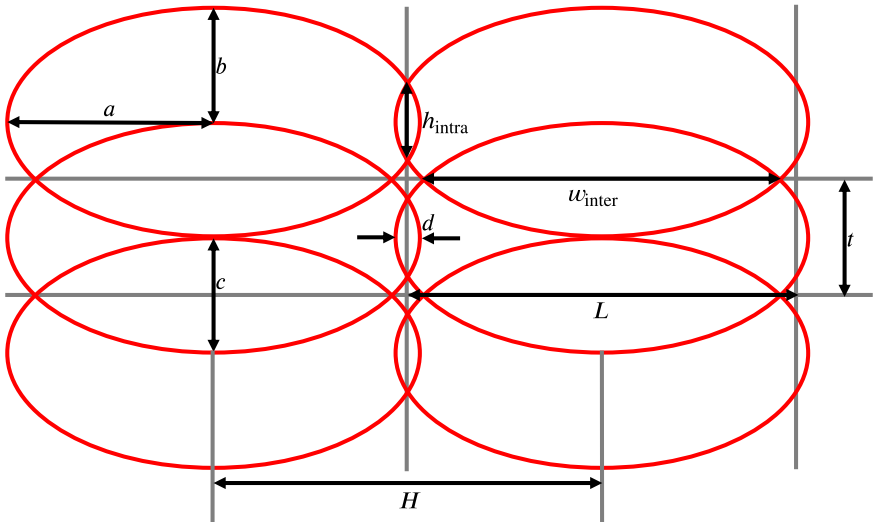

Fig. 7. Geometrical model describing the cross-sectional shape of 3D printed materials (from our previous work [28], based on models by Ahn et al. [27] & [26]). Build direction is vertical.

From the bond stress–slip results in Fig. 8 it can be observed that the bond strength between FDM 3D printed ABS and cementitious matrix is very low, i.e. below 1 MPa. Because all experiments resulted in successful bar pull-out, the weak bonding can be attributed to the fact that, at the molecular scale, ABS consists of hydrophobic groups [35]. As a result, there is no chemical adhesion with the cementitious mortar. Because of the absence of chemical adhesion, the bond strength mainly reflects the contribution of friction.

To better understand the bond behaviour between the FDM 3D printed ABS and cementitious matrix, SEM pictures are taken to visualize the interface amongst the two materials. Fig. 4 depicts two 20.0 kV images at different magnifications of 100 and 1000, clearly showing the elliptical morphology at the edges of the ABS 3D print. Furthermore, Fig. 4 shows that the cementitious mortar has completely filled the sharp interior portions at the intersections between the stacked bead layers. This raised the hypothesis

Table 3
Average input measurements for geometrical model from our previous work [28].

Input parameters	Dimensions (mm)	Standard deviation (mm)
a	0.3864	
b	0.1111	
c	0.0722	
d	0.1728	
h_{intra}	0.14	0.006
w_{inter}	0.57	0.027
t	0.15	0.006
L	0.6	0.027
H	0.6	0.027

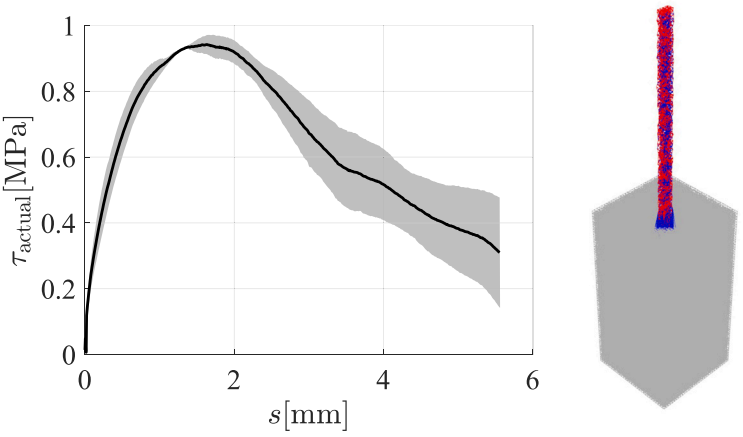

Fig. 8. Experimental pull-out bond stress–slip curves and numerical failure mode showing damage in blue.

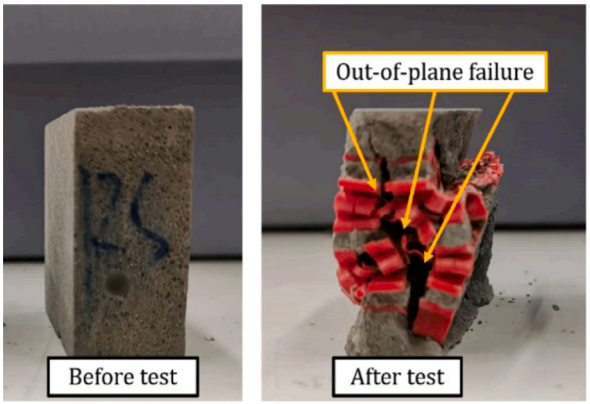

Fig. 9. Auxetic cementitious composite specimens before and after uniaxial compression tests [4].

that interlocking effects as a result of the 3D printing technique could be facilitated, particularly in the inter-layer direction which has a strong resemblance with deformed reinforcement bars. Nevertheless, aside from potentially elevating the ABS-matrix bond, the interlocking matrix could also induce deterioration: If the elliptical edges of the ABS 3D print are pushed into the cementitious matrix (or vice versa), the matrix could act like a splitting wedge leading to separation of the 3D printed layers. This may cause out-of-plane failure of the weak inter-layer bond within ABS 3D printed reinforcement as observed in [4] (i.e. adhesion failure among different printed layers), see Fig. 9.

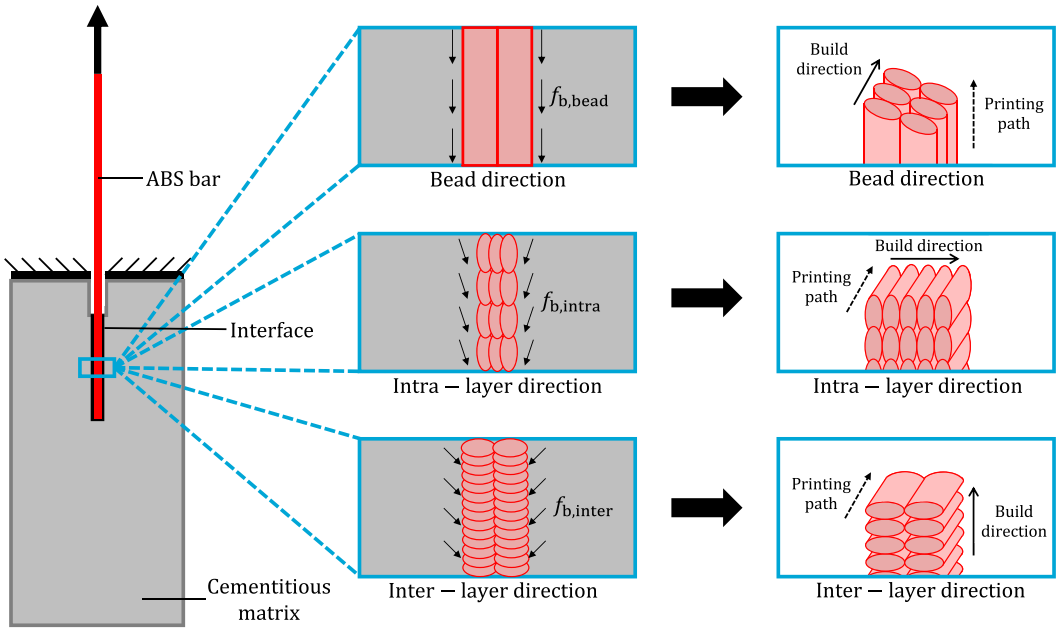

Fig. 10. Bond behaviour of hypothesized mechanical interactions caused by different (local) shapes of reinforcements depending on printing path and build direction.

Fig. 10 illustrates the bond behaviour of the hypothesized mechanical interactions for the three different directions as a result of morphological effects. Please note that the intra-layer and inter-layer directions are only investigated numerically at the micro-scale. These two directions can be regarded as if the ABS bars in the experiment were printed in the two mutually orthogonal build directions with respect to the bead direction.

3.2. Numerical simulations on two length scales

3.2.1. Lattice beam model

In LBM simulations, a specimen is discretized into a network of lattice beam elements which enable load transfer [29,33,52]. As the ratio between length and cross-sectional size of the lattice beams is usually small, Timoshenko beam elements are applied to consider shear contributions [53–55]. These models are particularly useful to study and incorporate microstructural information from a material [56] by means of overlapping the lattice mesh on top of (experimentally) obtained microstructures [57]. The model is able to simulate quasi-brittle (or even ductile) behaviour at the global level, even though local input properties usually prescribe a brittle relationship [29,58,59]. The mesh can be made irregular and distinct input properties can be given to different elements [60], thereby including heterogeneity. Different constitutive relationships can be implemented [33], e.g. linear-elastic [29,51,59] or non-linear [34,52,61]. The fracture process is captured via element removal, which may be lead by (step by step [29]) impairment of the element's stiffness [62]. After successful applications of LBM for materials such as concrete [57,63], having multiple phases (e.g. aggregates, cementitious mortar and interface [56] or ITZ [64]), the anisotropy present in FDM 3D printed polymers and reinforcement (e.g. intra-layer and inter-layer bonds [20]) was recently modelled through LBM by Bol et al. [28].

The fracture process is initiated through the application of a certain load (i.e. deformation or force controlled), after which a linear elastic analysis is performed. During the analysis, stresses are recorded in all beam elements and assessed against a predefined failure criterion (e.g. strength, strain, or energy [59]). If one of the elements reaches the criterion it is removed from the lattice network, thereby imposing damage. At this time, the load level and displacement field are saved before reloading the updated (i.e. damaged) mesh and redoing the aforementioned procedure. The analyses continue through deleting elements exceeding the failure criterion one by one until the modelled specimen fails. The damage's intention is to replicate crack initiation and propagation. All linear-elastic analyses combined constitute a non-linear analysis containing detailed cracking information [29,59]. The following stress evaluation takes place in all of the lattice beam elements [19,53,55,59,65–67]:

$$\sigma = \alpha_{\mathrm{N}} \frac{N}{A} + \alpha_{\mathrm{M}} \frac{\max\left(|M_i|, |M_j|\right)}{W}, \tag{3}$$

where N is the normal force, A the cross-sectional area, M_i and M_j are the local bending moments in nodes i and j, W is the section modulus, α_{N} and α_{M} are the normal force and bending moment influence factors, respectively. Based on our previous study [28], α_{N} and α_{M} are taken as 1.0 and 0.05, respectively. In this work, the failure criterion is defined based on strength, i.e. stress ($\mathbb{F}(\sigma)$):

$$\mathbb{F}(\sigma) = \frac{\sigma}{f_{\mathrm{y}}} \leq 1, \tag{4}$$

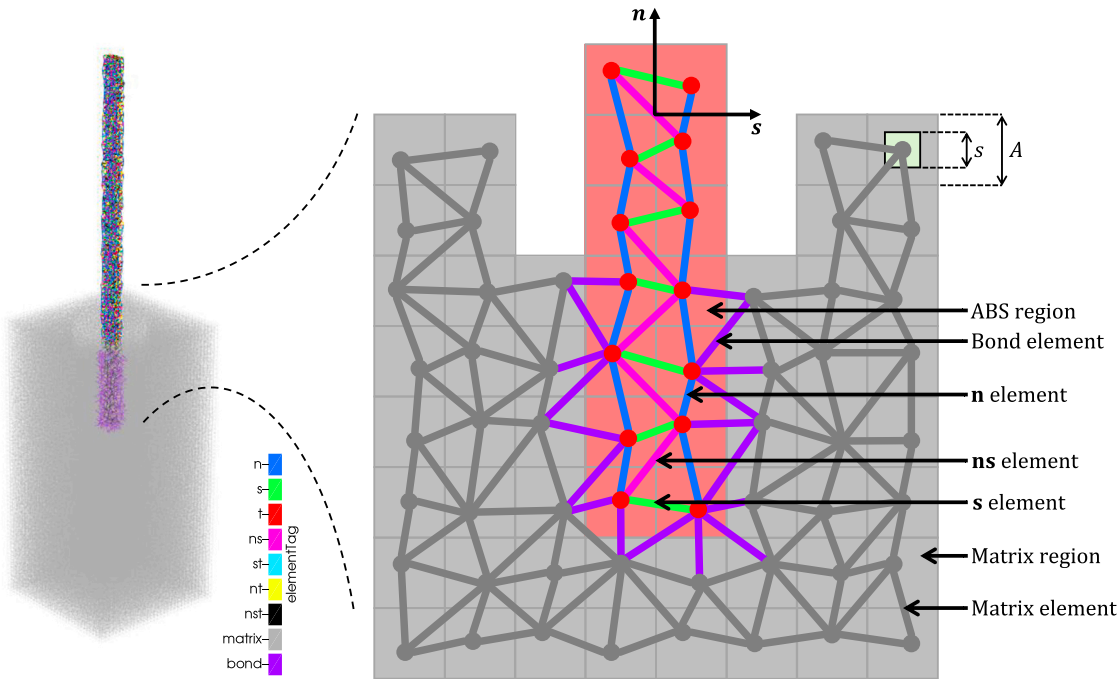

Fig. 11. Generated lattice mesh for meso-scale pull-out model.

where σ is the stress computed using Eq. (3) and f_y the material's strength. If one of the elements reaches the failure criterion in Eq. (4), i.e. $\mathbb{F}(\sigma) = 1$, this element is removed from the latte network as explained before.

Realistic mechanical and fracture responses were obtained through LBM by Xu et al. [19] for FDM 3D printed specimens subjected to uniaxial tension. Therein, the anisotropy caused by the manufacturing technique was captured implicitly. Our previous work [28] successfully improved upon this by explicitly modelling the anisotropy as a result of the intra-layer and inter-layer bonds present in FDM 3D printed polymers. More recently, Xu et al. [35] implemented experimentally validated properties for the bond behaviour between FDM 3D printed ABS and cementitious matrix. However, their LBM simulations assumed the 3D printed bars, as well as the interface among the two materials, to be homogeneous and isotropic. Therefore, the LBM simulations presented herein can be regarded as an extension of our previous model in [35] through incorporation of the anisotropic response observed in FDM 3D printed polymers. In this study, the hypothesis that morphological effects as a result of the 3D printing technique may have an beneficial effect on the bond behaviour between FDM 3D printed (auxetic) reinforcement and cementitious matrix will be tested. The numerical procedure used here is similar to that of our previous work [28], but will be briefly explained next:

- The test specimen is discretized by a grid of cubic cells with length A as shown in Fig. 11.
- Inside all cells, sub-cells having length s are created provided $0 \leq s \leq A$, see Fig. 11. Every sub-cell contains one lattice node at a random location within its volume. Hence, $R = s/A$ defines the randomness of the lattice mesh, thereby including heterogeneity. In this work, R equals 0.5, except for lattice nodes at boundary conditions (i.e. load application and support locations). Boundary nodes have zero randomness to ensure even load distribution.
- Neighbouring lattice nodes are connected by means of lattice beam elements along the three main axes (XX, YY, and ZZ), planar diagonals (XY, YZ, and XZ), and spatial diagonals (XYZ). To prevent intersecting diagonals, only the shortest are maintained.
- The phase of each lattice beam element is determined using two strategies, depending on the location of its two end nodes. The first strategy takes care that if both end nodes are located in the same region, the lattice beam element receives material properties belonging to that region (i.e. cementitious matrix in Fig. 11). When the two end nodes are in different regions, such that the element crosses between them, it is considered an interfacial element having properties corresponding to that particular interface (i.e. ABS-matrix bond in Fig. 11). The second strategy, proposed in [28], only concerns elements with both end nodes inside 3D printed material (i.e. ABS region in Fig. 11). In that case, mechanical properties are assigned based on the element's orientation with respect to the printing path (n_i in Fig. 11).
- Calibrations for each phase's stiffness and strength are performed as described in [28] by means of an iterative determination procedure shortly explained in Sections 3.2.2 and 3.2.3. For the constitutive relationships, multi-linear curves are used such that the elemental stiffness and strength are gradually altered during the analyses as illustrated in Fig. 12.

The same directional element domain discretization strategies as elaborated in [28] are used to capture the anisotropic behaviour of the ABS material as a result of the FDM 3D printing technique. Printing path-dependent lattice properties are assigned by

Table 4
Directional element domains for printing path-dependent property assignment from our previous work [28].

Directions	θ_{nst} (rad)	ϕ_{nst} (rad)
n	$\left[0, \frac{1}{8}\pi\right] \cup \left[\frac{7}{8}\pi, \frac{9}{8}\pi\right] \cup \left[\frac{15}{8}\pi, 2\pi\right)$	$\left[\frac{3}{8}\pi, \frac{5}{8}\pi\right]$
s	$[0, 2\pi)$	$\left[0, \frac{1}{8}\pi\right] \cup \left[\frac{7}{8}\pi, \pi\right]$
t	$\left[\frac{3}{8}\pi, \frac{5}{8}\pi\right] \cup \left[\frac{11}{8}\pi, \frac{13}{8}\pi\right]$	$\left[\frac{3}{8}\pi, \frac{5}{8}\pi\right]$
ns	$\left(0, \frac{1}{8}\pi\right) \cup \left(\frac{7}{8}\pi, \frac{9}{8}\pi\right) \cup \left(\frac{15}{8}\pi, 2\pi\right)$	$\left(\frac{1}{8}\pi, \frac{3}{8}\pi\right) \cup \left(\frac{5}{8}\pi, \frac{7}{8}\pi\right)$
st	$\left(\frac{3}{8}\pi, \frac{5}{8}\pi\right) \cup \left(\frac{11}{8}\pi, \frac{13}{8}\pi\right)$	$\left(\frac{1}{8}\pi, \frac{3}{8}\pi\right) \cup \left(\frac{5}{8}\pi, \frac{7}{8}\pi\right)$
nt	$\left(\frac{1}{8}\pi, \frac{3}{8}\pi\right) \cup \left(\frac{5}{8}\pi, \frac{7}{8}\pi\right) \cup \left(\frac{9}{8}\pi, \frac{11}{8}\pi\right) \cup \left(\frac{13}{8}\pi, \frac{15}{8}\pi\right)$	$\left(\frac{3}{8}\pi, \frac{5}{8}\pi\right)$
nst	$\left(\frac{1}{8}\pi, \frac{3}{8}\pi\right) \cup \left(\frac{5}{8}\pi, \frac{7}{8}\pi\right) \cup \left(\frac{9}{8}\pi, \frac{11}{8}\pi\right) \cup \left(\frac{13}{8}\pi, \frac{15}{8}\pi\right)$	$\left(\frac{1}{8}\pi, \frac{3}{8}\pi\right) \cup \left(\frac{5}{8}\pi, \frac{7}{8}\pi\right)$

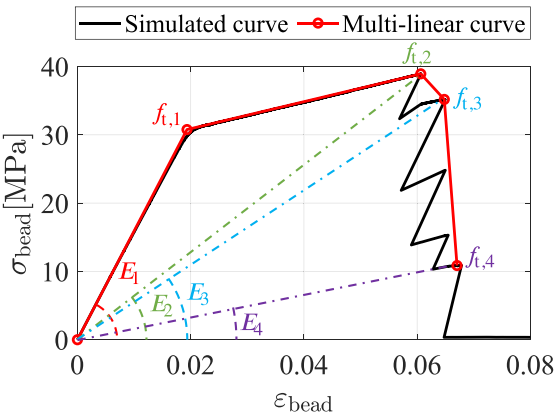

Fig. 12. Multi-linear constitutive relationship for 3D printed ABS in uniaxial bead or **n** direction following Table 5 from our previous work [28].

introducing a local coordinate system consisting of unit vectors n_i, s_i and t_i. As shown in Fig. 11, n_i corresponds to the ABS bar's longitudinal axis, which is parallel to the printing path, whilst s_i is perpendicular to n_i and lies in the same plane. t_i is the normal vector of this plane and is therefore not depicted in the two-dimensional representation in Fig. 11. Directional element categories are imposed in every local coordinate system by means of spherical angles, where θ_{nst} is the azimuth angle of the projection on the plane formed by unit vectors n_i and t_i, measured from vector n_i, and ϕ_{nst} is the polar angle measured from the unit vector s_i. Now, the directional element categories can be decomposed into directional element domains in the local coordinate system with respect to the spherical angles. The decomposed directional element domains are listed in Table 4. Each colour of the lattice beam elements in Fig. 11 corresponds to a different constitutive relationship. The input properties for the lattice beam elements corresponding to matrix phase are calibrated according to the experimental data presented in [4].

3.2.2. Modelling procedure

The generated lattice mesh for the meso-scale pull-out simulations is displayed in Fig. 11, having a mesh size of 0.6 mm that is chosen to match the dimensions of a cubical Representative Volume Element (RVE) of FDM 3D printed ABS material from our previous study [28]. This RVE is calibrated based on microstructural experimental analysis to explicitly include the anisotropy present in FDM 3D printed material caused by the layer-by-layer deposition process [20]. Hence, it provides the constitutive relationships based on the beam element's orientation with respect to the printing path (n_i in Fig. 11) [28]. The input parameters for the ABS filament in the LBM simulations presented here can therefore be directly adopted from [28], which are provided in Table 5. The matrix phase input is calibrated according to the standard procedure for LBM simulations [28], which entails the beam element radii and their local strength: First the element radii are iteratively determined in order to have matching local and global Young's moduli, followed by setting the local strength input such that the material's global strength matches experimental observations in the same manner. As pointed out before, the input properties for the lattice beam elements corresponding to matrix phase are calibrated according to the experimental data presented in [4]. With the bond phase being the only unknown, the meso-scale model allows for calibration of the ABS-mortar bond properties through parameter fitting.

Once the ABS-mortar bond properties at the meso-scale are fitted with the experimental pull-out results, these are scaled down to the micro-scale. To enable explicit modelling of the microstructural morphology as a result of the FDM 3D printing technique (see [20]), a very fine mesh is required that would yield too computationally expensive numerical simulations at the meso-scale [35]. Therefore, taking into account the geometrical analyses described in [20] and Fig. 4, three different directions with respect to the

Table 5
Printing path-dependent directional element properties from our previous work [28].

Properties (MPa)	n	s	t	ns	st	nt	nst
E_1	1590	1570	1584	1912	1912	1923	2430
G_1	530	523.33	528	637.33	637.33	641	81
$f_{t,1}$	30.77	4.57	22.03	4.58	4.58	22.86	6.93
$f_{c,1}$	−38.46	−5.71	−27.54	−5.73	−5.73	−28.58	−8.66
E_2	642		980	812	789	775	1313
G_2	214		326.67	270.67	263	258.33	437.67
$f_{t,2}$	38.93		14.31	1.96	1.90	9.38	3.75
$f_{c,2}$	−48.66		−17.89	−2.45	−2.38	−11.73	−4.69
E_3	543			780	776	776	1256
G_3	181			260	258.67	258.67	418.67
$f_{t,3}$	35.18			15.39	10.74	15.26	22.06
$f_{c,3}$	−43.98			−19.24	−13.43	−19.08	−27.58
E_4	162			313	580	346	598
G_4	54			104.33	193.33	115.33	199.33
$f_{t,4}$	10.86			19.65	8.16	18.72	10.51
$f_{c,4}$	−13.58			−24.56	−10.20	−23.40	−13.14
E_5				275	90	295	514
G_5				91.67	30	98.33	171.33
$f_{t,5}$				17.49	1.28	18.43	15.28
$f_{c,5}$				−21.86	−1.60	−23.04	−19.10
E_6				82		89	211
G_6				27.33		29.67	70.33
$f_{t,6}$				5.34		6.12	19.44
$f_{c,6}$				−6.68		−7.65	−24.30
E_7							59
G_7							19.67
$f_{t,7}$							6.09
$f_{c,7}$							−7.61

printing path will be studied by means of micro-scale LBM simulations: (i) the bead or filament direction (parallel to the printing path, n_i), (ii) the intra-layer direction (t_i), and (iii) the inter-layer direction (s_i). These are the three mutually orthogonal print configurations in extrusion-based 3D printing, such as FDM, which is the method applied here. Particularly the inter-layer direction has a strong resemblance with deformed reinforcement bars, see Fig. 4.

The bead direction is the only direction that was successfully tested by means of pull-out experiments. It is therefore assumed that the bond behaviour between ABS and cementitious matrix is the same in terms of chemical adhesion and friction. Accordingly, morphological effects only contribute to the mechanical interaction through anchorage or interlocking of the mortar and elliptical edges.

3.2.3. Micro-scale pull-out models

At the micro-scale, a mesh size of 25 μm is used throughout all models. Similar to Section 3.2.2, this matches with the discretization used for the ABS cubical RVE in our previous study [28]. Therefore, the experimentally calibrated microstructural constitutive relationships used therein can be directly adopted too (see Table 7). The out-of-plane model thickness is set to 750 μm with a matrix width kept constant at 1000 μm. All other dimensions related to the ABS bar correspond to the microstructural experimental analysis performed in [28] and are modelled via Rhinoceros® using Grasshopper according to the geometrical models by Ahn et al. [27] and its extension in [26] (see Fig. 7 and Table 3). The cementitious matrix is calibrated using the same iterative procedure as described in Section 3.2.2 for finding the element radii and local strength input at the micro-scale, according to the experimental data presented in [4]. The local strength input parameters for the ABS-mortar bond elements is scaled accordingly.

To reduce computational costs only a half of each cutout is modelled in view of symmetry. To approximate experimental conditions, the loading and constraints are directly applied to the cutout portions of the ABS and surrounding matrix. In total, four scenarios are modelled at the micro-scale: a reference for the intra-layer direction which mimics the bead direction (Fig. 13(a)), the intra-layer direction containing two adjacent beads (Fig. 13(b)), a reference for the inter-layer direction that reflects the bead direction (Fig. 13(c)), and the inter-layer direction consisting of eight stacked layers (Fig. 13(d)). Because the semi-minor axis of the elliptic cross-section in the intra-layer direction (i.e. b in Fig. 7) is smaller compared to the semi-major axis in the inter-layer direction (i.e. a in Fig. 7), there is less polymer phase (i.e. ABS) in the micro-scale pull-out models for the intra-layer compared to the inter-layer (see Fig. 13). Due to this difference in dimensions, as well as the randomness of the lattice mesh, a reference simulation for each direction is required to make a fair comparison. Hence, the two references in Fig. 13(a) and (c) reflecting the bead direction are there to prevent any mesh dependencies when comparing the reference and morphological featured cases for the intra-layer and inter-layer, respectively.

3.2.4. Micro-scale push-out models

Another methodology to test micromechanical bond behaviour is the push-out test [68] (see Section 2.2). This procedure allows to see the isolated effect of morphological features without any influence of the intra-layer and inter-layer bonds within the 3D printed

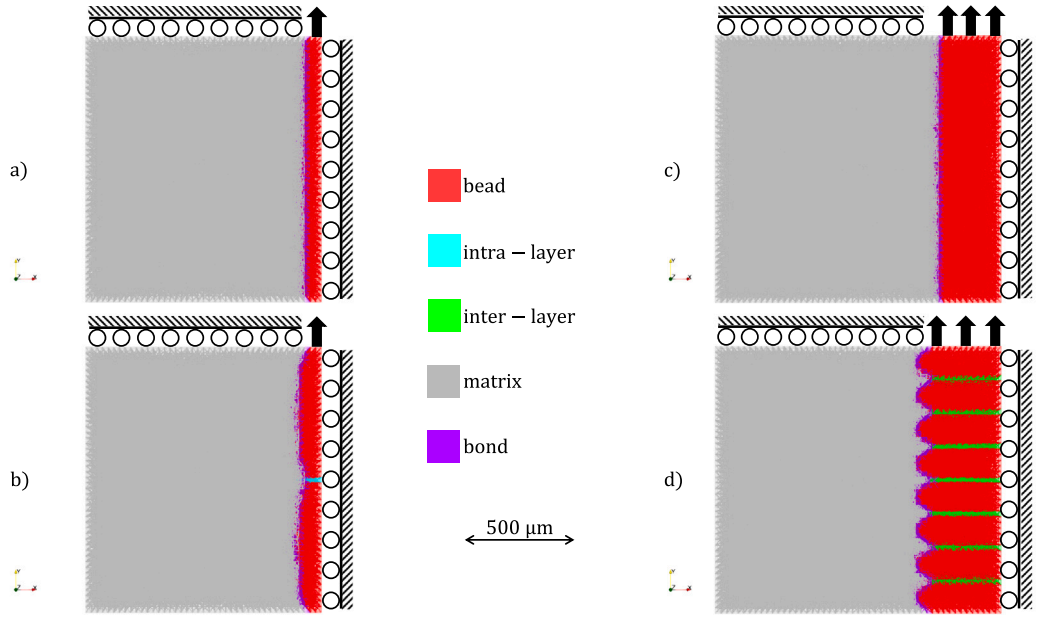

Fig. 13. Generated lattice meshes for micro-scale pull-out models of (a) intra-layer reference, (b) intra-layer direction, (c) inter-layer reference, and (d) inter-layer direction.

ABS material. By exposing the reinforcement to compression, tensile failure of the internal bonds will not be governing. Hence, given the same experimentally-fitted bond properties as before, the push-out tests can measure the contribution of mechanical interactions. Similar to the micro-scale pull-out simulations, LBM push-out simulations are performed on the same small virtual cutouts from the experimental setup as displayed in Fig. 10. The only difference with the models in Fig. 13 are the boundary conditions, which are modified to simulate push-out conditions. Four push-out scenarios are modelled in parallel at the micro-scale to prevent any interfacial failure modes: a reference for the intra-layer direction which mimics the bead direction (Fig. 14(a)), the intra-layer direction containing two adjacent beads (Fig. 14(b)), a reference for the inter-layer direction that reflects the bead direction (Fig. 14(c)), and the inter-layer direction consisting of eight stacked layers (Fig. 14(d)). Similar to the micro-scale pull-out models, the two references in Fig. 14(a) and (c) reflecting the bead direction are there to avoid mesh dependencies due to the randomness of the lattice mesh and the difference in dimensions amongst the intra-layer and inter-layer, respectively.

4. Results

4.1. Meso-scale bond stress–slip relationship

The meso-scale bond stress–slip relationship is fitted with experimental pull-out data, similar to [35]. The starting point is to model the ABS bar, which is done in accordance with the printing path-dependent two-scale modelling scheme data explained in [28]. The local input for the matrix phase is calibrated with experimental data in [4] and lattice properties used in [35], corresponding globally to mortar with a Young's modulus of 11 417 MPa. The local input therefore yields $E = 11\,417$ MPa, $G = 3805.7$ MPa, $f_t = 4.07$ MPa, and $f_c = -32.59$ MPa. Please note that local input (i.e. element properties) are always calibrated in such a way so that the global specimen response is achieved. Hence, depending on the mesh parameters (e.g. size and randomness), slightly different local properties are needed to mimic the same global behaviour [69].

The constitutive relationship for the bond elements between FDM 3D printed ABS bars and cementitious matrix is defined as a multi-linear curve composed of five segments (see Fig. 15), similar to the pull-out models developed in [35]. Hence, their stiffness and strength are modified accordingly throughout the analyses rather than being directly discarded. The input parameters for the bond phase regarding the meso-scale pull-out model in Fig. 11 are contained in Table 6. The values for the ABS bars from [28], including the directional discretizations to capture their anisotropy, can be found in Table 5.

The shape of the multi-linear constitutive relationship for ABS-mortar bond in Fig. 15 shows strong similarities with analytical models described in Section 2.3. It resembles the analytical model by Harajli et al. [40,47,50] displayed in Fig. 3. Other analytical models discussed in Section 2.3 contain strikingly equivalent (portions of these) shapes [39,49,70]. As explained in Section 2.1, the analytical model by Harajli et al. [40,47,50] has been implemented successfully before in LBM simulations for obtaining input parameters of interface elements between concrete and deformed reinforcement bars by Gu et al. [34]. The implemented multi-linear constitutive relation approximates the experimental curves in a realistic manner as shown in Fig. 16. The maximum bond stress that can be reached without breaking the ABS bar in the LBM simulations is 0.8 MPa, which is about 16% lower compared to the experimental data.

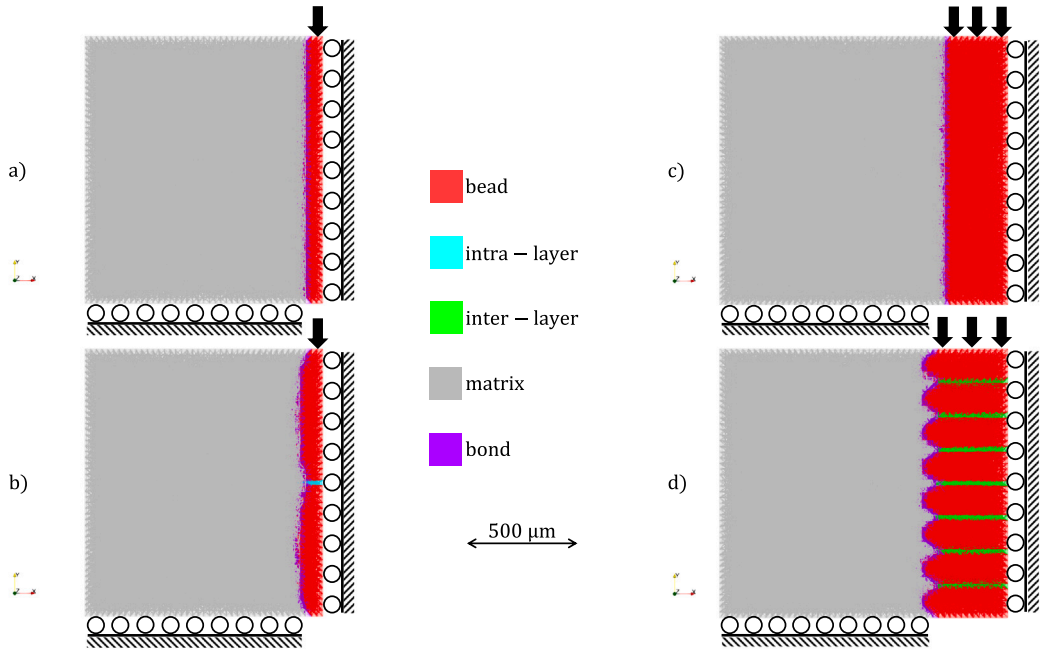

Fig. 14. Generated lattice meshes for micro-scale push-out models of (a) intra-layer reference, (b) intra-layer direction, (c) inter-layer reference, and (d) inter-layer direction.

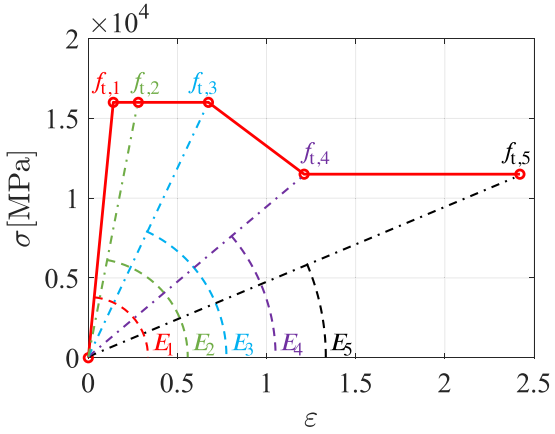

Fig. 15. Multi-linear constitutive relationship for ABS-mortar bond.

Table 6
Input parameters for meso-scale ABS-mortar bond phase elements, following the curve shown in Fig. 15.

Properties	Segment 1	Segment 2	Segment 3	Segment 4	Segment 5
E_i (MPa)	114 170	57 085	23 750	9 500	4 750
G_i (MPa)	38 057	19 028	7 917	3 167	1 583
$f_{t,i}$ (MPa)	16 000	16 000	16 000	11 500	11 500
$f_{c,i}$ (MPa)	−16 000	−16 000	−16 000	−11 500	−11 500

4.2. Micro-scale bond stress–slip analysis

Small virtual cutouts from the meso-scale pull-out experiments as described in Section 3.2.3 are subjected to LBM simulations of micro-scale pull-out tests. The micro-scale bond stress–slip relationships resulting from the four scenarios described therein are displayed in Fig. 17, maintaining the same format as Fig. 13. However, the micro-scale slip values in Fig. 17 cannot be compared

Table 7
Input parameters for micro-scale simulations.

Properties (MPa)	Bead	Inter-layer	Intra-layer	Matrix
E_1	1590	1590	1590	11 417
G_1	530	530	530	3805.7
$f_{t,1}$	40	6.6	29	4.23
$f_{c,1}$	−50	−8.25	−36.25	−33.84
E_2	343			
G_2	114.33			
$f_{t,2}$	38			
$f_{c,2}$	−47.5			

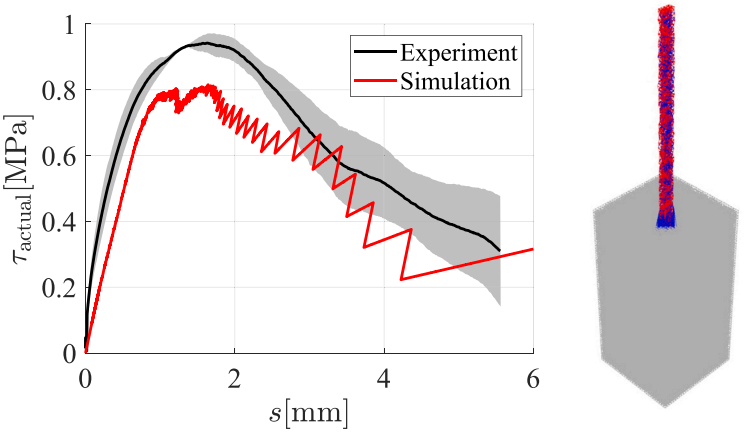

Fig. 16. Comparison of meso-scale pull-out bond stress–slip curves and failure mode showing damage in blue.

Table 8
Input parameters for micro-scale ABS-mortar bond phase elements.

Properties	Segment 1	Segment 2	Segment 3	Segment 4	Segment 5
E_i (MPa)	114 170	57 085	23 750	9500	4750
G_i (MPa)	38 057	19 028	7917	3167	1583
$f_{t,i}$ (MPa)	12 075	12 075	12 075	8682	8682
$f_{c,i}$ (MPa)	−12 075	−12 075	−12 075	−8682	−8682

to their meso-scale counterparts, because the latter include elastic deformation from the ABS bar whilst the former does not [71]. The micro-scale input for the bead, inter-layer and intra-layer phases is used from our previous work [28]. These are provided in Table 7, where the subscripts correspond to the segment number of a (multi-)linear curve (see Fig. 12).

The local input for the matrix phase is recalibrated for the different mesh size at the micro-scale. Compared to the meso-scale simulations, in the micro-scale simulations the local strength input parameters for the matrix (see Table 7) and ABS-mortar bond elements (see Table 8) are slightly reduced.

Fig. 17(a) shows the reference pull-out behaviour for the intra-layer direction model which reflects the bead direction and therefore directly corresponds to the experimental pull-out observations. It can be seen that the obtained bond strength of about 0.73 MPa is almost identical to the meso-scale pull-out results in Fig. 16 of about 0.8 MPa. This difference can be attributed to small differences in the lattice mesh because of its randomness. Moreover, the shape of the pull-out bond stress–slip curve and failure mode are similar to those obtained experimentally and numerically at the meso-scale (see Fig. 16). Please recall that the micro-scale slip values in Fig. 18 are not comparable to the meso-scale as the latter include elastic deformation from the ABS bar whilst the former does not [71]. Furthermore, Fig. 17(a) also includes the deformed mesh showing cracks in blue at final stage of the analysis which clearly indicates a clean pull-out response as observed during the experiments. Fig. 17(b) displays the intra-layer direction having a similar response with a slightly higher bond strength of nearly 0.84 MPa and also a clean pull-out. Fig. 17(c) depicts the reference pull-out behaviour for the inter-layer direction model which also corresponds to the bead direction. In this case, the obtained bond strength of 0.80 MPa perfectly matches the meso-scale pull-out results in Fig. 16 and the fracture of the model also clearly indicates a clean pull-out response as found during testing. However, Fig. 17(d) displays the inter-layer direction having a very sharp peak of nearly 1.14 MPa that can be attributed to the fact that the inter-layer bond inside the ABS bar fails. Hence, the matrix-reinforcement bond behaviour cannot be measured as there is no full pull-out in this case, i.e. the bond is too strong. The fact that the bar could not be pulled out validates the micro-scale model in a qualitative manner, as similar preliminary findings have been recorded. The directional-dependent bond behaviour of the intra-layer and inter-layer directions at the micro-scale can be related to that of the

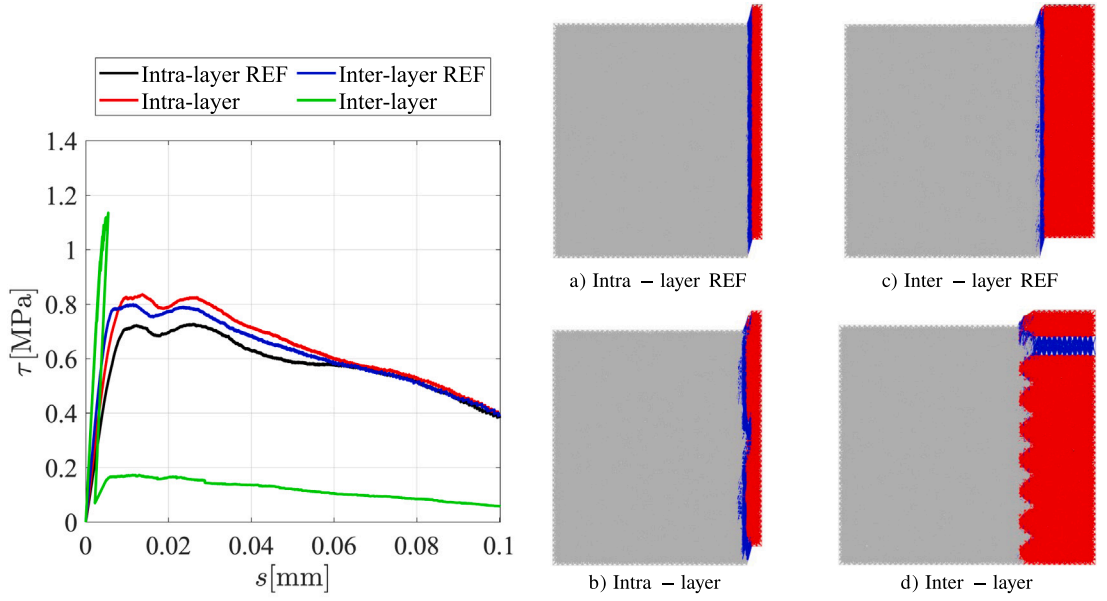

Fig. 17. Micro-scale pull-out simulation bond stress–slip and fracture results. Deformed meshes showing cracks in blue at final stage of the analyses.

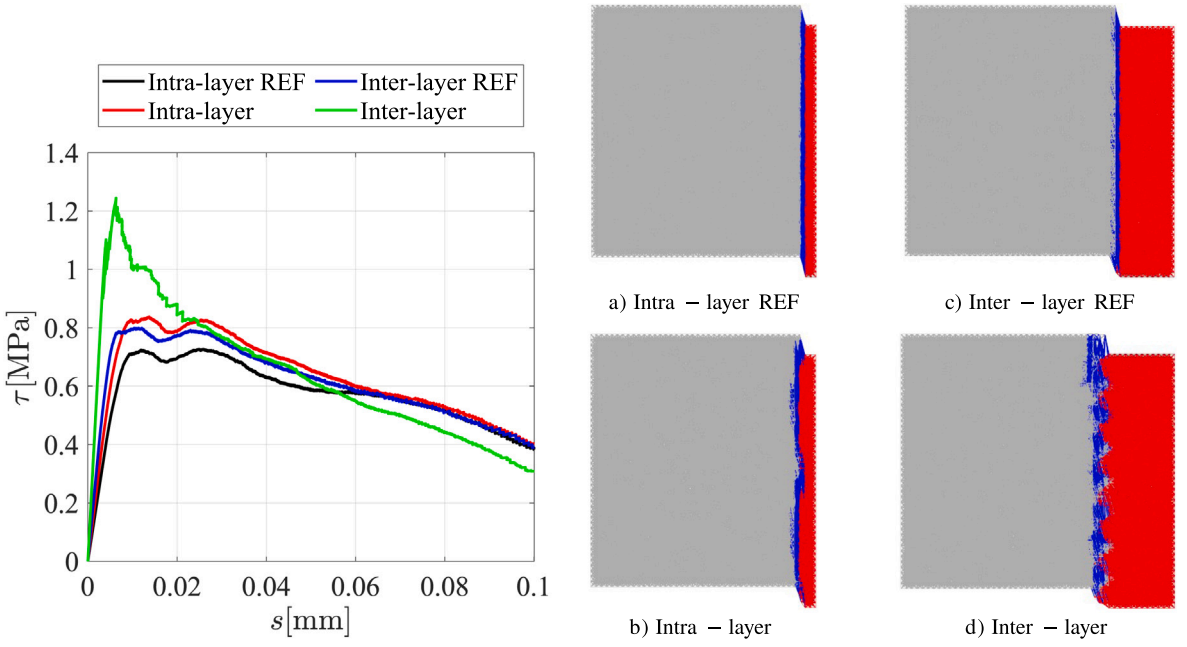

Fig. 18. Micro-scale push-out simulation bond stress–slip and fracture results. Deformed meshes showing cracks in blue at final stage of the analyses.

bead direction using a strength ratio:

$$r_{\mathrm{b},i} = \frac{f_{\mathrm{b},i}}{f_{\mathrm{b,bead}}}\,. \tag{5}$$

In Eq. (5), $f_{\mathrm{b},i}$ can be regarded as $f_{\mathrm{b,intra}}$ and $f_{\mathrm{b,inter}}$ corresponding to the bond strengths in the intra-layer and inter-layer directions at the micro-scale, respectively, and $f_{\mathrm{b,bead}}$ is the bond strength in the bead direction at the micro-scale. Considering the directional-dependencies described by Eq. (5), bond strength ratios of 1.15 and 1.56 are obtained for the intra-layer and inter-layer directions, respectively. Nevertheless, the inter-layer direction ratio does not constitute successful pull-out. Preliminary experimental results

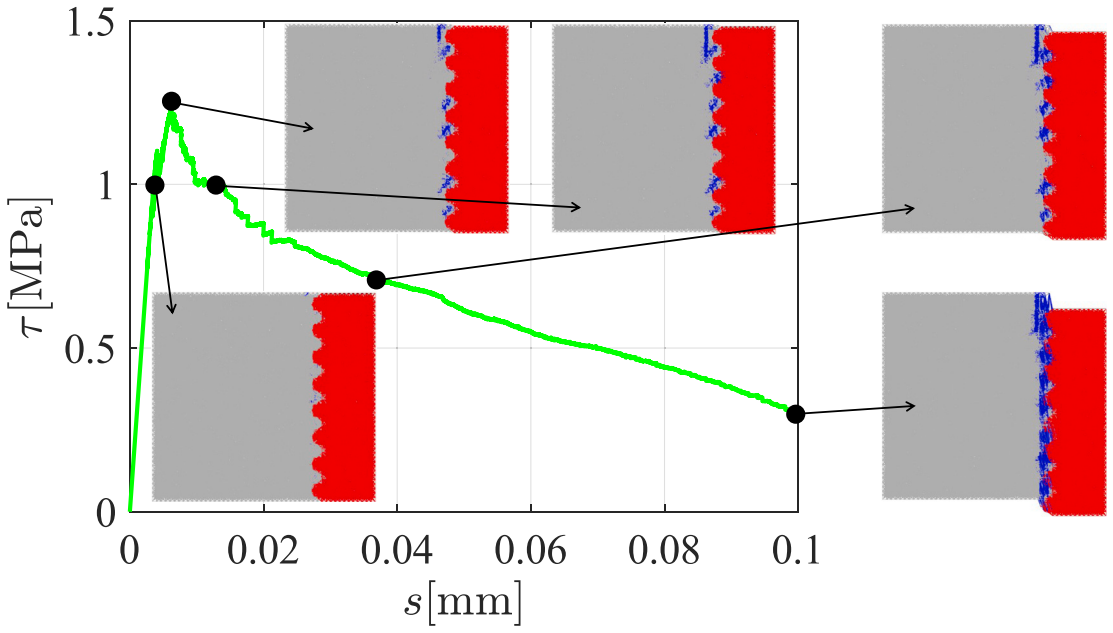

Fig. 19. Inter-layer push-out simulation damage evolution. Deformed meshes showing cracks in blue at indicated stages of the analysis.

have also shown that the inter-layer bonds present in the FDM 3D printed ABS are too weak and result in breakage of the filament instead of the bar pull-out. To see the actual bond behaviour in the inter-layer direction, micro-scale push-out simulations are needed.

Given the same experimentally-fitted bond properties provided earlier, micro-scale push-out simulations are used to purely measure the contribution of mechanical interactions without any interfacial failure modes. The same small virtual cutouts from the meso-scale pull-out tests are simulated, with the only difference being the boundary conditions as illustrated in Fig. 14. Again, resulting micro-scale bond stress–slip relationships are contained in Fig. 17, having the same format as the aforementioned figure. The exact same constitutive relation as in the LBM micro-scale pull-out simulations is used for the bond behaviour here.

Fig. 18(a) shows the push-out results for the intra-layer reference case. It is noteworthy that the bond strength perfectly matches the value of the micro-scale pull-out intra-layer reference (0.73 MPa). Additionally, the shape in Fig. 18(a) is identical to that of Fig. 17(a), which is in favour of the utilized numerical acquisition procedure of directional-dependent bond properties, irrespective of the boundary conditions (i.e. pull-out versus push-out). The fracture of the aforementioned case also constitutes a clean and successful push-out response. Similarly, Fig. 18(b) displays the intra-layer direction, again comprising a clean push-out with softening behaviour after reaching an identically increased bond strength of 0.84 MPa compared to Fig. 13(b). Fig. 18(c) depicts the inter-layer reference case where it is notable that the bond strength of 0.80 MPa is maintained once more, thereby exactly matching the bond strength values of both the meso-scale and micro-scale pull-out LBM results. The model's fracture behaviour also indicates a clean push-out response. Where the inter-layer direction failed prematurely under pull-out conditions, Fig. 18(d) displays a successful push-out in which the inter-layer bond within the ABS bar survives. Even though the peak is not as smooth as the others in Fig. 18, a bond strength of about 1.24 MPa is reached. Therefore, this result truly shows the isolated effect of morphological features without any influence of the intra-layer and inter-layer bonds within the 3D printed ABS material. It can also be observed in Fig. 19(d) that due to the wedging of the morphological features, some splitting of the matrix occurs. As a result, the aforementioned bond stress–slip curve looks similar in shape as the monotonic envelope for splitting failure displayed in Fig. 3. Finally, revisiting the bond strength ratios in Eq. (5) that relate the directional-dependent bond behaviour of the intra-layer and inter-layer directions to that of the bead direction at the micro-scale, the intra-layer and inter-layer directions yield values of 1.15 and 1.56, respectively.

5. Discussion

In this study, it is hypothesized that the elliptical geometry resulting from 3D printing may enhance the bond strength between the polymeric reinforcement and cementitious matrix. This is based on the following considerations:

1. From literature on reinforced concrete (i.e., with steel reinforcement, see Section 2.1) it is known that the bond comprises three components: Chemical (adhesive) bond, frictional bond and physical bond. The former two are geometry independent, whilst the latter is strongly dependent on the geometry. This is why ribbed reinforcement bars have stronger bond and, consequently, shorter transfer length than plain reinforcement bars.

2. In our previous work on ABS reinforcement [51], we observed that intentionally adding ribs on 3D printed reinforcement meshes enhances the bonding by physical interlocking.

To conclusively support the hypothesis, additional experimental investigations are necessary for validation purposes. Specifically, the effect of the different geometrical configurations should be quantified (e.g., elliptic versus plain). Although it is acknowledged that specific experiments relating the polymer geometry with the bond strength are not present, the authors have shown in the past that LBM simulations as used herein are able to replicate the experimentally observed geometrical surface configurations in concrete/concrete repair systems without any additional parameters, see Luković et al. [72]. In that work, simulations of the direct shear test clearly showed that rough surface results in a higher strength compared to smooth surface, simply as a result of the geometry of the bond.

In the current work, a similar approach was taken with the first step being meso-scale pull-out simulations to determine the bond stress–slip curve between the 3D printed polymer bars and the cementitious matrix. This resulted in Fig. 8, which holds for the "bead" printing direction (i.e., flat bond between the polymer and the matrix, see Fig. 10). The bond was also tested for the inter-layer direction, but proved to be too strong: The reinforcement broke, and the pull-out curve could not be measured. Nevertheless, from the pull-out curves of the "bead direction" printed bars, micro-scale adhesive bond properties could be determined, which hold for any printing direction. Since the only difference between the printing directions is the geometry, these properties could be confidently used to simulate the bond behaviour for the other printing directions (i.e., with elliptical bond instead of "flat"), as shown in Luković et al. [72].

A comparison between experimental pull-out tests and numerical results is given in Fig. 16. As explained above, for other printing directions (inter-layer and intra-layer), the bond was too strong (i.e., the reinforcement too weak) to perform a successful pull-out test due to rupture of the reinforcement. This clearly does not allow quantitative comparison with the simulations: However, such behaviour is clearly expected based on the modelling work presented here. Based on the discussion above, the modelling framework entails a high level of confidence. Nonetheless, developing a dedicated small-scale setup for testing the bond strength between the polymeric reinforcement and cementitious matrix will be the focus of future research.

6. Summary and conclusions

The bond behaviour between cementitious mortar (i.e. matrix) and 3D printed polymers (e.g. Acrylonitrile Butadiene Styrene (ABS)) has been studied using the Lattice Beam Model (LBM) on two length scales. To numerically investigate the hypothesis that morphological features as a result of the Fused Deposition Modelling (FDM) 3D printing technique may enhance the bond, the first step was to use pull-out experiments to calibrate a replica meso-scale model by means of parameter fitting. This model provided constitutive relationships at the meso-scale which served as a reference for micro-scale models that explicitly capture the directional-dependent mechanical interaction coming from geometrical features at the edges of FDM 3D printed parts. The anisotropy present in FDM 3D printed reinforcement (i.e. intra-layer and inter-layer bonds) was modelled according to our previous work, but the ABS-matrix bond was calibrated in the current study. By explicitly modelling the geometry, and without changing input parameters, we learned what effect printing direction has on the bond between 3D printed polymeric reinforcement and cementitious matrix. Because of premature pull-out failure of the ABS bar in the inter-layer direction, push-out micro-scale models are considered in parallel to measure the contribution purely related to mechanical interactions. Their results will be used to inform specimen-scale models for simulating the composite behaviour of Auxetic Cementitious Composites (ACCs). The properties of the ABS material for both the meso-scale and micro-scale models discussed here are directly adopted from earlier developed printing path-dependent two-scale models.

From the presented work, it can be concluded that push-out models are needed to see the actual bond behaviour between cementitious matrix and FDM 3D printed ABS bars in the inter-layer printing direction. In this direction, pull-out models are found unable to reach full bond failure without breaking the inter-layer bond present within FDM 3D printed ABS. The interlocking effects as a result of the 3D printing technique in the inter-layer direction show to be significant, seeing a bond strength increase of 56% with respect to the (reference) bead direction (i.e. the 'bulk material' without interfaces perpendicular to the loading direction). However, these mechanical interaction effects in the intra-layer direction are found to be much smaller with a bond strength increase of only 15% compared to the reference direction. Finally, the hypothesized directional-dependent bond behaviour as a result of morphological features at the edges of FDM 3D printed ABS has been quantified and proven to exist.

CRediT authorship contribution statement

Rowin J.M. Bol: Writing – original draft, Visualization, Validation, Software, Methodology, Conceptualization. **Yading Xu:** Writing – review & editing, Resources, Investigation. **Mladena Luković:** Writing – review & editing, Methodology. **Branko Šavija:** Writing – review & editing, Supervision, Project administration, Funding acquisition, Conceptualization.

Declaration of competing interest

The authors declare the following financial interests/personal relationships which may be considered as potential competing interests: Branko Savija reports financial support was provided by European Research Council. If there are other authors, they declare that they have no known competing financial interests or personal relationships that could have appeared to influence the work reported in this paper.

Acknowledgements

Funding: This work was supported by the European Research Council (ERC) [grant number 101041342].

Data availability

Data will be made available on request.

References

[1] Y. Xu, H. Zhang, Y. Gan, B. Šavija, Cementitious composites reinforced with 3D printed functionally graded polymeric lattice structures: Experiments and modelling, Addit. Manuf. 39 (2021) http://dx.doi.org/10.1016/j.addma.2021.101887.
[2] S. Qin, S. Cao, E. Yilmaz, J. Li, Influence of types and shapes of 3D printed polymeric lattice on ductility performance of cementitious backfill composites, Constr. Build. Mater. 307 (2021) http://dx.doi.org/10.1016/j.conbuildmat.2021.124973.
[3] C. Tang, J. Liu, W. Hao, Y. Wei, Flexural properties of 3D printed graded lattice reinforced cementitious composites using digital image correlation, Mater. Des. 227 (2023) http://dx.doi.org/10.1016/j.matdes.2023.111734.
[4] Y. Xu, B. Šavija, Auxetic cementitious composites (ACCs) with excellent compressive ductility: Experiments and modeling, Mater. Des. 237 (2024) 112572, http://dx.doi.org/10.1016/j.matdes.2023.112572, [Online]. Available: https://linkinghub.elsevier.com/retrieve/pii/S0264127523009887.
[5] T.C. Lim, Analogies across auxetic models based on deformation mechanism, Phys. Status Solidi - Rapid Res. Lett. 11 (2017) http://dx.doi.org/10.1002/pssr.201600440.
[6] J.J. Warner, A.R. Gillies, H.H. Hwang, H. Zhang, R.L. Lieber, S. Chen, 3D-printed biomaterials with regional auxetic properties, J. Mech. Behav. Biomed. Mater. 76 (2017) 145–152, http://dx.doi.org/10.1016/j.jmbbm.2017.05.016.
[7] S. Maran, I.G. Masters, G.J. Gibbons, Additive manufacture of 3d auxetic structures by laser powder bed fusion—design influence on manufacturing accuracy and mechanical properties, Appl. Sci. (Switzerland) 10 (2020) 1–19, http://dx.doi.org/10.3390/app10217738.
[8] M.S. Rad, Y. Prawoto, Z. Ahmad, Analytical solution and finite element approach to the 3D re-entrant structures of auxetic materials, Mech. Mater. 74 (2014) 76–87, http://dx.doi.org/10.1016/j.mechmat.2014.03.012.
[9] A. Joseph, V. Mahesh, D. Harursampath, On the application of additive manufacturing methods for auxetic structures: a review, Adv. Manuf. 9 (2021) 342–368, http://dx.doi.org/10.1007/s40436-021-00357-y.
[10] K.E. Evans, A. Alderson, Auxetic materials: Functional materials and structures from lateral thinking!, Adv. Mater. 12 (2000) 617–628.
[11] V.A. Lvov, F.S. Senatov, A.A. Stepashkin, A.A. Veveris, M.D. Pavlov, A.A. Komissarov, Low-cycle fatigue behavior of 3D-printed metallic auxetic structure, Mater. Today: Proc. 33 (2020) 1979–1983, http://dx.doi.org/10.1016/j.matpr.2020.06.130.
[12] C.-H. Hsueh, S. Schmauder, C.-S. Chen, K.K. Chawla, N. Chawla, W. Chen, Y. Kagawa, Handbook of Mechanics of Materials, Springer Nature Singapore Pte Ltd., 2019, http://dx.doi.org/10.1007/978-981-10-6884-3.
[13] J. Carlos, A. Elipe, A.D. Lantada, Comparative study of auxetic geometries by means of computer-aided design and engineering, Smart Mater. Struct. 21 (2012).
[14] H.M. Kolken, K. Lietaert, T. van der Sloten, B. Pouran, A. Meynen, G.V. Loock, H. Weinans, L. Scheys, A.A. Zadpoor, Mechanical performance of auxetic meta-biomaterials, J. Mech. Behav. Biomed. Mater. 104 (2020) http://dx.doi.org/10.1016/j.jmbbm.2020.103658.
[15] X.T. Wang, B. Wang, X.W. Li, L. Ma, Mechanical properties of 3D re-entrant auxetic cellular structures, Int. J. Mech. Sci. 131–132 (2017) 396–407, http://dx.doi.org/10.1016/j.ijmecsci.2017.05.048.
[16] T. Li, Y. Chen, X. Hu, Y. Li, L. Wang, Exploiting negative Poisson's ratio to design 3D-printed composites with enhanced mechanical properties, Mater. Des. 142 (2018) 247–258, http://dx.doi.org/10.1016/j.matdes.2018.01.034.
[17] Y. Xu, H. Zhang, E. Schlangen, M. Luković, B. Šavija, Cementitious cellular composites with auxetic behavior, Cem. Concr. Compos. 111 (2020) http://dx.doi.org/10.1016/j.cemconcomp.2020.103624.
[18] Y. Xu, E. Schlangen, M. Luković, B. Šavija, Tunable mechanical behavior of auxetic cementitious cellular composites (CCCs): Experiments and simulations, Constr. Build. Mater. 266 (2021) http://dx.doi.org/10.1016/j.conbuildmat.2020.121388.
[19] Y. Xu, H. Zhang, B. Šavija, S.C. Figueiredo, E. Schlangen, Deformation and fracture of 3D printed disordered lattice materials: Experiments and modeling, Mater. Des. 162 (2019) 143–153, http://dx.doi.org/10.1016/j.matdes.2018.11.047.
[20] R.J.M. Bol, B. Šavija, Micromechanical models for FDM 3D-printed polymers: A review, Polymers 15 (2023) 4497, http://dx.doi.org/10.3390/polym15234497, [Online]. Available: https://www.mdpi.com/2073-4360/15/23/4497.
[21] H.R. Dana, F. Barbe, L. Delbreilh, M.B. Azzouna, A. Guillet, T. Breteau, Polymer additive manufacturing of ABS structure: Influence of printing direction on mechanical properties, J. Manuf. Process. 44 (2019) 288–298, http://dx.doi.org/10.1016/j.jmapro.2019.06.015.
[22] S. Paul, Finite element analysis in fused deposition modeling research: A literature review, Meas.: J. Int. Meas. Confed. 178 (2021) http://dx.doi.org/10.1016/j.measurement.2021.109320.
[23] J.C. Riddick, M.A. Haile, R.V. Wahlde, D.P. Cole, O. Bamiduro, T.E. Johnson, Fractographic analysis of tensile failure of acrylonitrile-butadiene-styrene fabricated by fused deposition modeling, Addit. Manuf. 11 (2016) 49–59, http://dx.doi.org/10.1016/j.addma.2016.03.007.
[24] M.E. Haque, D. Banerjee, S.B. Mishra, B.K. Nanda, A numerical approach to measure the surface roughness of FDM build part, Mater. Today: Proc. 18 (2019) 5523–5529, [Online]. Available: www.sciencedirect.comwww.materialstoday.com/proceedings2214-7853.
[25] A. Armillotta, Simulation of edge quality in fused deposition modeling, Rapid Prototyp. J. 25 (2019) 541–554, http://dx.doi.org/10.1108/RPJ-06-2018-0151.
[26] L. Di Angelo, P. Di Stefano, A. Marzola, Surface quality prediction in FDM additive manufacturing, Int. J. Adv. Manuf. Technol. 93 (2017) 3655–3662, http://dx.doi.org/10.1007/s00170-017-0763-6.
[27] D. Ahn, J.H. Kweon, S. Kwon, J. Song, S. Lee, Representation of surface roughness in fused deposition modeling, J. Mater. Process. Technol. 209 (2009) 5593–5600, http://dx.doi.org/10.1016/j.jmatprotec.2009.05.016.
[28] R.J.M. Bol, Y. Xu, B. Šavija, Printing path-dependent two-scale models for 3D printed planar auxetics by material extrusion, Addit. Manuf. 89 (2024) http://dx.doi.org/10.1016/j.addma.2024.104293.
[29] M. Luković, H. Dong, B. Šavija, E. Schlangen, G. Ye, K.V. Breugel, Tailoring strain-hardening cementitious composite repair systems through numerical experimentation, Cem. Concr. Compos. 53 (2014) 200–213, http://dx.doi.org/10.1016/j.cemconcomp.2014.06.017.
[30] M. Lukovic, Y. Yang, E. Schlangen, D. Hordijk, On the Potential of Lattice Type Model for Predicting Shear Capacity of Reinforced Concrete and SHCC Structures, fib. The International Federation for Structural Concrete, 2018, pp. 804–813, http://dx.doi.org/10.1007/978-3-319-59471-2_94.
[31] J.E. Bolander, S. Saito, Fracture analyses using spring networks with random geometry, Eng. Fract. Mech. 61 (1998) 569–591.
[32] J. Kang, K. Kim, Y.M. Lim, J.E. Bolander, Modeling of fiber-reinforced cement composites: Discrete representation of fiber pullout, Int. J. Solids Struct. 51 (2014) 1970–1979, http://dx.doi.org/10.1016/j.ijsolstr.2014.02.006.

[33] S. Mustafa, S. Singh, D. Hordijk, E. Schlangen, M. Luković, Experimental and numerical investigation on the role of interface for crack-width control of hybrid SHCC concrete beams, Eng. Struct. 251 (2022) http://dx.doi.org/10.1016/j.engstruct.2021.113378.
[34] D. Gu, S. Mustafa, J. Pan, M. Luković, Reinforcement-concrete bond in discrete modeling of structural concrete, Comput.- Aided Civ. Infrastruct. Eng. (2022) http://dx.doi.org/10.1111/mice.12937.
[35] Y. Xu, Z. Wan, B. Šavija, Elevating mechanical performance of cementitious composites with surface-modified 3D-printed polymeric reinforcements, Dev. Built Environ. 19 (2024) http://dx.doi.org/10.1016/j.dibe.2024.100522.
[36] E. Monaldo, S. Marfia, Modelling of damage and plasticity phenomena in 3D printed materials via a multiscale approach, Eur. J. Mech. A Solids (2023) 105140, http://dx.doi.org/10.1016/j.euromechsol.2023.105140.
[37] T. Hyatt, An Account of Some Experiments with Portland-Cement-Concrete Combined with Iron, as a Building Material, Chiswick Press, London, 1877, p. 47.
[38] D. Abrams, Tests of bond between concrete and steel, 1913.
[39] M.F. Bado, J.R. Casas, G. Kaklauskas, Distributed sensing (DOFS) in reinforced concrete members for reinforcement strain monitoring, crack detection and bond-slip calculation, Eng. Struct. 226 (2021) http://dx.doi.org/10.1016/j.engstruct.2020.111385.
[40] M.H. Harajli, Effect of confinement using steel, FRC, or FRP on the bond stress-slip response of steel bars under cyclic loading, Mater. Struct./ Mater. Constr. 39 (2006) 621–634, http://dx.doi.org/10.1617/s11527-005-9054-z.
[41] U. Farooq, H. Nakamura, T. Miura, Y. Yamamoto, Proposal of bond behavior simulation model by using discretized voronoi mesh for concrete and beam element for reinforcement, Cem. Concr. Compos. 110 (2020) http://dx.doi.org/10.1016/j.cemconcomp.2020.103593.
[42] S.M. Mirza, J. Houde, Study of bond stress-slip relationships in reinforced concrete, ACI J. 76 (1979) 19–46, http://dx.doi.org/10.14359/6935.
[43] L.A. Lutz, P. Gergely, Mechanics of bond and slip of deformed bars in concrete, ACI J. 64 (1967) 711–721, http://dx.doi.org/10.14359/7600.
[44] ACI Committee 408, Bond stress-the state of the art, J. Am. Concr. Inst. 63 (1966) 1161–1190, http://dx.doi.org/10.14359/7665.
[45] ACI Committee 408, 408R-03: Bond and development of straight reinforcing bars in tension, 2003, p. 49.
[46] G. Xing, C. Zhou, T. Wu, B. Liu, Experimental study on bond behavior between plain reinforcing bars and concrete, Adv. Mater. Sci. Eng. 2015 (2015) http://dx.doi.org/10.1155/2015/604280.
[47] M.H. Harajli, M. Hout, W. Jalkh, Local bond stress-slip behavior of reinforcing bars embedded in plain and fiber concrete, ACI J. 92 (1995) 343–353, http://dx.doi.org/10.14359/999.
[48] P. Namakiaraghi, A. Sadighi, R. Spragg, A.R. Najafi, Y.A. Farnam, Towards development of cement-based composites reinforced with architected 3D-printed polymers, Constr. Build. Mater. 422 (2024) http://dx.doi.org/10.1016/j.conbuildmat.2024.135838.
[49] R. Eligehausen, E.P. Popov, V.V. Bertéro, Local bond stress-slip relationships of deformed bars under generalized excitations, in: Proceedings of the 7th European Conference on Earthquake Engineering, 1982, pp. 69–80, http://dx.doi.org/10.18419/opus-415, [Online]. Available: https://www.researchgate.net/publication/279507857.
[50] M.H. Harajli, Bond stress-slip model for steel bars in unconfined or steel, FRC, or FRP confined concrete under cyclic loading, J. Struct. Eng. 135 (2009) 509–518, http://dx.doi.org/10.1061/ASCE0733-94452009135:5509.
[51] Y. Xu, B. Šavija, Development of strain hardening cementitious composite (SHCC) reinforced with 3D printed polymeric reinforcement: Mechanical properties, Compos. Part B: Eng. 174 (2019) http://dx.doi.org/10.1016/j.compositesb.2019.107011.
[52] B. Šavija, G.E. Smith, D. Liu, E. Schlangen, P.E. Flewitt, Modelling of deformation and fracture for a model quasi-brittle material with controlled porosity: Synthetic versus real microstructure, Eng. Fract. Mech. 205 (2019) 399–417, http://dx.doi.org/10.1016/j.engfracmech.2018.11.008.
[53] Z. Chang, H. Zhang, E. Schlangen, B. Šavija, Lattice fracture model for concrete fracture revisited: Calibration and validation, Appl. Sci. (Switzerland) 10 (2020) http://dx.doi.org/10.3390/app10144822.
[54] N. Jiang, H. Zhang, Z. Chang, E. Schlangen, Z. Ge, B. Šavija, Discrete lattice fracture modelling of hydrated cement paste under uniaxial compression at micro-scale, Constr. Build. Mater. 263 (2020) http://dx.doi.org/10.1016/j.conbuildmat.2020.120153.
[55] Z. Chang, H. Zhang, M. Liang, E. Schlangen, B. Šavija, Numerical simulation of elastic buckling in 3D concrete printing using the lattice model with geometric nonlinearity, Autom. Constr. 142 (2022) http://dx.doi.org/10.1016/j.autcon.2022.104485.
[56] J. Tejchman, J. Kozicki, Experimental and Theoretical Investigations of Steel-Fibrous Concrete, 2010 ed., Springer-Verlag, Berlin, 2010.
[57] Z. Qian, Multiscale modeling of fracture processes in cementitious materials, 2012.
[58] D. Liu, B. Šavija, G.E. Smith, P.E. Flewitt, T. Lowe, E. Schlangen, Towards understanding the influence of porosity on mechanical and fracture behaviour of quasi-brittle materials: experiments and modelling, Int. J. Fract. 205 (2017) 57–72, http://dx.doi.org/10.1007/s10704-017-0181-7.
[59] B. Šavija, M. Luković, J. Pacheco, E. Schlangen, Cracking of the concrete cover due to reinforcement corrosion: A two-dimensional lattice model study, Constr. Build. Mater. 44 (2013) 626–638, http://dx.doi.org/10.1016/j.conbuildmat.2013.03.063.
[60] H. Zhang, Y. Xu, Y. Gan, Z. Chang, E. Schlangen, B. Šavija, Combined experimental and numerical study of uniaxial compression failure of hardened cement paste at micrometre length scale, Cem. Concr. Res. 126 (2019) http://dx.doi.org/10.1016/j.cemconres.2019.105925.
[61] B. Šavija, D. Liu, G. Smith, K.R. Hallam, E. Schlangen, P.E. Flewitt, Experimentally informed multi-scale modelling of mechanical properties of quasi-brittle nuclear graphite, Eng. Fract. Mech. 153 (2016) 360–377, http://dx.doi.org/10.1016/j.engfracmech.2015.10.043.
[62] N. Jiang, Z. Ge, Y. Guan, Z. Zuo, H. Zhang, Y. Ling, B. Šavija, Experimentally validated meso-scale fracture modelling of foamed concrete, Theor. Appl. Fract. Mech. 122 (2022) http://dx.doi.org/10.1016/j.tafmec.2022.103631.
[63] M. Yip, Z. Li, B.S. Liao, J.E. Bolander, Irregular lattice models of fracture of multiphase particulate materials, Int. J. Fract. 140 (2006) 113–124, http://dx.doi.org/10.1007/s10704-006-7636-6.
[64] G. Lilliu, 3D analysis of fracture processes in concrete, 2007.
[65] Z. Chang, E. Schlangen, B. Šavija, Extended Lattice Model to Simulate the Printing Process of 3D Printed Cementitious Materials, in: RILEM Bookseries, vol. 28, Springer, 2020, pp. 814–823, http://dx.doi.org/10.1007/978-3-030-49916-7_80.
[66] Z. Chang, H. Zhang, E. Schlangen, B. Šavija, Z.E. Chang, Lattice model for numerical analysis of fracture process of concrete material under various loading conditions, 2019, [Online]. Available: https://www.researchgate.net/publication/335305423.
[67] Y. Xu, Architected cementitious cellular materials towards auxetic behavior, 2021, http://dx.doi.org/10.4233/uuid:1a9e29a6-4868-4096-bc88-a1095cf568d3, [Online]. Available: https://doi.org/10.4233/uuid:1a9e29a6-4868-4096-bc88-a1095cf568d3.
[68] S. Robuschi, J. Sumearll, I. Fernandez, K. Lundgren, Bond of naturally corroded, plain reinforcing bars in concrete, Struct. Infrastruct. Eng. 17 (2021) 792–808, http://dx.doi.org/10.1080/15732479.2020.1768273.
[69] A. Delaplace, R. Desmorat, Discrete 3D model as complimentary numerical testing for anisotropic damage, Int. J. Fract. 148 (2007) 115–128, http://dx.doi.org/10.1007/s10704-008-9183-9.
[70] S.W. Lee, S.B. Kang, K.H. Tan, E.H. Yang, Experimental and analytical investigation on bond-slip behaviour of deformed bars embedded in engineered cementitious composites, Constr. Build. Mater. 127 (2016) 494–503, http://dx.doi.org/10.1016/j.conbuildmat.2016.10.036.
[71] Y. Gan, M. Liang, E. Schlangen, K. van Breugel, B. Šavija, Two scale models for fracture behaviours of cementitious materials subjected to static and cyclic loadings, Constr. Build. Mater. 426 (2024) 136107, http://dx.doi.org/10.1016/j.conbuildmat.2024.136107, [Online]. Available: https://linkinghub.elsevier.com/retrieve/pii/S0950061824012480.
[72] M. Lukovic, E. Schlangen, G. Ye, B. Šavija, in: J.V. Mier, G. Ruiz, C. Andrade, R. Yu, X. Zhang (Eds.), Impact of surface roughness on the debonding mechanism in concrete repairs, Ciudad Real, 2013.